

A Straight-Forward Method of Moments Procedure to Solve the Time Domain Integral Equation Applicable to PEC Bodies via Triangular Patch Modeling

Sadasiva M. Rao

Naval Research Laboratory
Washington DC 20375, USA

Abstract – In this work, a simple and straight-forward method of moments solution (MOM) procedure is presented to obtain the induced current distribution on an arbitrarily-shaped conducting body illuminated by a Gaussian plane wave directly in the time domain using a patch modeling approach. The method presented in this work, besides being stable, is also capable of handling multiple excitation pulses of varying frequency content incident from different directions in a trivial manner. The method utilizes standard Rao-Wilton-Glisson (RWG) functions and simple triangular functions for the space and time variables, respectively, for both expansion and testing. The method adopts conventional MOM and requires no further manipulation invariably needed in standard time-marching methods. The moment matrix generated via this scheme is a block-wise Toeplitz matrix and, hence, the solution is extremely efficient. The method is validated by comparing the results with the data obtained from the frequency domain solution. Several simple and complex numerical results are presented to validate the procedure.

Index Terms – Electromagnetic fields, Integral equations, Method of moments, Numerical methods, Time Domain.

I. INTRODUCTION

In recent times, the transient analysis of electromagnetic scattering has received a great deal of attention. With the advent of faster computers and an increase of memory space, many scattering problems of complex objects are being performed directly in the time domain because of the generation of a broad-band data in a single simulation. Further, the direct time domain (TD) techniques provide an opportunity to observe and interpret electromagnetic scattering behavior.

Some of the early analytical work in transient

electromagnetic problems were based on physical optics to obtain the approximate impulse response from conducting flat plates, spheres, and prolate spheroids [1]. A time domain solution for an infinite cylindrical antenna was performed by Wu in 1961 [2]. Next, Bennett derived an integro-differential equation applicable to a perfectly conducting square plate by enforcing the boundary condition on the electric field and then solved directly in the time domain [3]. Bennett labeled this technique as the space-time integral-equation (STIE) technique. The STIE method discretizes the scatterer into square patches, the time axis divided into equal increments, and the currents at each instant are determined by the knowledge of the incident field and currents at previous instants.

Next, we note that the STIE solution methodology has been applied to many different geometrical shapes, simple as well as complex, and now is known as the Marching-on-in-Time (MOT) method [4]. Although MOT algorithm is popular, it is prone to late-time instabilities with growing oscillations as time progresses which makes the technique unreliable. Unfortunately, most of the proposed remedies to either arrest these oscillations or eliminate them completely, work only for simple problems, and invariably fail for complex objects. In the last 20 years, there has been an explosion of proposed remedies with limited success and only a few selected publications are cited here for completeness [5-19].

Recently, a new type of algorithm was applied to wire-grid models of arbitrary bodies to solve the time domain integral equation (TDIE) using the method of moments (MOM) [20] and [21]. The numerical procedure presented in [21] and [22] is not a MOT scheme and there is no time marching involved. We solve the integral equation over a space-time grid, and hence no error accumulation as happens in MOT schemes. This procedure eliminates marching-on-in-time altogether, remains stable and

also ideally suited to handle a large number of excitations in a trivial manner. In the present work, we apply this procedure to perfectly electric conducting (PEC) bodies via planar triangular patch modeling.

Next, we further note that the present method is not either explicit or implicit methods commonly available to solve the time-domain integral equation [4]. In our view, both the explicit and the implicit methods are related to Marching-on-in-Time (MOT) method. The only difference being the length of the time step. If the time step is smaller than the smallest spatial distance between the spatial basis functions, R_{min} , then we have explicit scheme. Otherwise we have implicit scheme. In both cases, the solution is achieved by time marching method. In such a scheme, currents are evaluated at the first time instant, $t_1 = \Delta t$ by solving the governing equation and, using this knowledge, move to obtain currents at the second time instant $t_2 = 2\Delta t$. Next, proceed to obtain currents at 3rd, 4th, and later time instants in a similar way. Obviously, these methods are prone to error accumulation which is avoided in the present work.

In the following section, we present the detailed mathematical steps describing the algorithm. In Section III, we present numerical solution scheme and several important guidelines to apply the procedure successfully. In Section IV, we present several numerical results to test the validity of the technique. Finally, Section V discusses important conclusions along with possible improvements and future work to be undertaken in this area.

II. INTEGRAL EQUATION FORMULATION

Let S denote an open or closed perfectly conducting arbitrarily-shaped body as shown in Fig. 1, illuminated by a time-domain pulse. An electric field $\mathbf{E}^i(\mathbf{r}, t)$, defined in the absence of the scatterer, is incident on and induces a surface current $\mathbf{J}(\mathbf{r}, t)$ on S . Using basic mathematical steps outlined in [4], the scattered electric field $\mathbf{E}^s(\mathbf{r}, t)$ computed from the surface current is given by:

$$\mathbf{E}^s(\mathbf{r}, t) = -\frac{\partial \mathbf{A}(\mathbf{r}, t)}{\partial t} - \nabla \Phi(\mathbf{r}, t), \quad (1)$$

where the magnetic vector potential and the electric scalar potentials are given by:

$$\mathbf{A}(\mathbf{r}, t) = \mu \int_S \frac{\mathbf{J}(\mathbf{r}', t - \frac{R}{c})}{4\pi R} dS', \quad (2)$$

and

$$\Phi(\mathbf{r}, t) = \frac{1}{\epsilon} \int_S \frac{q_s(\mathbf{r}', t - \frac{R}{c})}{4\pi R} dS'. \quad (3)$$

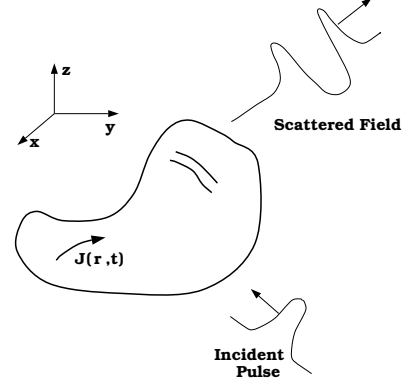


Fig. 1. An arbitrary body illuminated by a Gaussian plane wave.

In Eqs. (2) and (3), $R = |\mathbf{r} - \mathbf{r}'|$, μ and ϵ denote the permeability and permittivity of the surrounding medium, respectively, \mathbf{r} and \mathbf{r}' are the locations of the observation and source points on S and c is the velocity of the electromagnetic wave. The surface charge density q_s is related to the induced current \mathbf{J} by the continuity equation given by,

$$\nabla_s \cdot \mathbf{J} = -\frac{\partial q_s}{\partial t}. \quad (4)$$

Differentiating Eq. (3) with respect to time and using Eq. (4), we obtain the following expression for the time derivative of the scalar potential as:

$$\Psi \triangleq \frac{\partial \Phi}{\partial t} = \frac{-1}{\epsilon} \int_\ell \frac{\nabla_s \cdot \mathbf{J}(\mathbf{r}', t - R/c)}{4\pi R} dS'. \quad (5)$$

Next, an integro-differential equation for \mathbf{J} can be derived using the boundary condition ($\mathbf{E}^i + \mathbf{E}^s)_{tan} = 0$ on S as:

$$\left[\frac{\partial \mathbf{A}}{\partial t} + \nabla \Phi \right]_{tan} = \mathbf{E}_{tan}^i. \quad (6)$$

The charge density appearing in the scalar potential of Eq. (6) may be eliminated by differentiating Eq. (6) with respect to time and using Eq. (5). Thus, the popular electric field integral equation (EFIE) for an arbitrarily-shaped conducting body in time domain is given by:

$$\left[\frac{\partial^2 \mathbf{A}}{\partial t^2} + \nabla \Psi \right]_{tan} = \left[\frac{\partial \mathbf{E}^i}{\partial t} \right]_{tan}, \quad (7)$$

which needs to be solved for the unknown current $\mathbf{J}(\mathbf{r}, t)$.

III. NUMERICAL SOLUTION SCHEME

The first step in the numerical scheme is to describe adequately the given geometry to the digital

computer. This task is most easily accomplished by covering the body surface with planar triangular patches to generate a “patch model” of the given body. We choose the planar triangular patches to model the body because they have the ability to conform to any geometrical surface or boundary. In fact, simple as well as complex bodies, can be easily modeled by planar triangular patches and can be described to the computer using automated schemes. Further, for numerical purposes, it is very easy to increase the patch density in areas where more resolution is required.

Next, we note that the triangular mesh consists of several electrically short patches, mutually attached to each other to approximate the given body. The common edge where several patches are attached is known as an *interior edge*. If only one patch is attached to an edge, then that edge is referred to as a *boundary edge* and removed from the solution scheme. When only two triangular patches are attached to a given edge, that interior edge is referred to as an *ordinary edge* and one unknown is associated with this edge. Further, if more than two triangular patches are attached to a given edge, then we have a *junction edge* and the number of unknowns associated with this junction edge is one less than the total number of patches connected to this edge.

The next task in the numerical solution procedure is to develop an algorithm to solve the integral equation (7). We accomplish this task by selecting the well-known method of moments [22].

A. Definition of space and time basis functions

Assuming that the body is modeled with triangular patches, we use the well-known Rao-Wilton-Glisson (RWG) functions [23] for expansion and testing of space variables. Referring to Fig. 2, the RWG function for any edge m common to the two triangles T_m^\pm is given by,

$$\mathbf{f}_m(\mathbf{r}) = \begin{cases} \frac{l_m}{2A_m^+} \boldsymbol{\rho}_m^+ & \text{for } \mathbf{r} \in T_m^+ \\ \frac{l_m}{2A_m^-} \boldsymbol{\rho}_m^- & \text{for } \mathbf{r} \in T_m^- \\ 0 & \text{otherwise.} \end{cases} \quad (8)$$

In Eq. (8), l_m denotes the length of the m^{th} edge and A_m^\pm is the area of triangle T_m^\pm . Further, an arbitrary point in T_m^+ may be located by the position vector \mathbf{r} , relative to the origin, O , or by $\boldsymbol{\rho}_m^+$, referenced at the free vertex of T_m^+ . For an arbitrary point in T_m^- , the position vector $\boldsymbol{\rho}_m^-$ is similarly defined except that it is directed toward the free vertex of T_m^- . The “+” or “-” convention is determined by

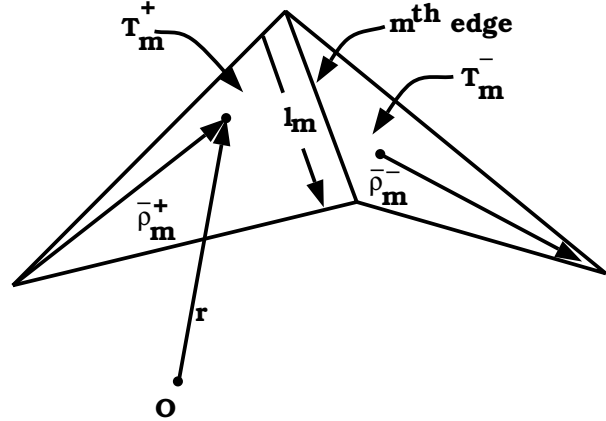


Fig. 2. Triangle pair and geometrical parameters associated with the m^{th} interior edge.

choosing a reference direction for positive current flow for the m^{th} edge. This current is assumed to flow from T_m^+ to T_m^- . Also, we follow the convention where superscripts refer to the faces and subscripts refer to the edges. For example, T_m^+ is the positive triangle associated with edge m .

Now, let us define the triangle functions for the time variable. In order to do so, let us first define an upper limit on the time variable $t = T$, where T represents the time when the incident pulse becomes negligible. Then, we divide the time axis $0 \rightarrow T$ into N_t uniform time intervals given by Δt and denote $t_n = n\Delta t$ for $n = 1, 2, \dots, N_t$. We note that, initially, the MOM scheme is applied to a finite interval $0 \rightarrow T$. We also note that extending the time interval to later times is trivial and discussed later. The mathematical description of the triangle function for the time variable is given as,

$$g_n(t) \equiv \begin{cases} 1 - \frac{|t-t_n|}{\Delta t} & t \in (t_{n-1}, t_{n+1}) \\ 0 & \text{otherwise.} \end{cases} \quad (9)$$

Next, we approximate the induced current $\mathbf{J}(\mathbf{r}, t)$ as:

$$\mathbf{J}(\mathbf{r}, t) \approx \sum_{m=1}^{N_S} \sum_{n=1}^{N_t} I_{m,n} \mathbf{f}_m(\mathbf{r}) g_n(t), \quad (10)$$

where N_S and N_t represent the number of basis (expansion) functions in space and time, respectively. Thus, for a complex body approximated by a triangular mesh, we have N_S space basis functions including basis functions associated with junction edges, N_t time functions. Thus, a straight forward MOM application results in $P = N_S \times N_t$ unknowns to be evaluated. The MOM procedure to obtain each unknown by solving Eq. (7) is described in the following:

B. Testing procedure

Considering the Galerkin testing procedure, we use the same functions defined in Eqs. (8) and (9) for testing of space and time variables, respectively. Defining

$$\begin{aligned} & \langle \mathbf{f}_m(\mathbf{r})g_n(t), \mathbf{F}(\mathbf{r}, t) \rangle = \\ & \int_S \int_T \mathbf{f}_m(\mathbf{r})g_n(t) \bullet \mathbf{F}(\mathbf{r}, t) dS dt, \end{aligned} \quad (11)$$

we can write Eq. (7) as:

$$\begin{aligned} & \langle \mathbf{f}_m(\mathbf{r})g_n(t), \left[\frac{\partial^2 \mathbf{A}}{\partial t^2} + \nabla \Psi \right] \rangle = \\ & \langle \mathbf{f}_m(\mathbf{r})g_n(t), \left[\frac{\partial \mathbf{E}^i}{\partial t} \right] \rangle \end{aligned} \quad (12)$$

for $m = 1, 2, \dots, N_S$ and $n = 1, 2, \dots, N_t$. Further, we can rewrite Eq. (12) as,

$$\begin{aligned} & \int_t g_n(t) \frac{\partial^2}{\partial t^2} \int_S [\mathbf{f}_m(\mathbf{r}) \bullet \mathbf{A}(\mathbf{r}, t) dS] dt \\ & + \int_t g_n(t) \int_S [\mathbf{f}_m(\mathbf{r}) \bullet \nabla \Psi(\mathbf{r}, t) dS] dt \\ & = \int_t g_n(t) \int_S \left[\mathbf{f}_m(\mathbf{r}) \bullet \frac{\partial \mathbf{E}^i(\mathbf{r}, t)}{\partial t} dS \right] dt. \end{aligned} \quad (13)$$

Now, using the well-known integration by parts scheme on the first integral of Eq. (13) and using Eq. (9), we can re-write Eq. (13) as:

$$\begin{aligned} & \int_S \mathbf{f}_m(\mathbf{r}) \bullet \\ & \left[\frac{\mathbf{A}(\mathbf{r}, t_{n+1}) - 2\mathbf{A}(\mathbf{r}, t_n) + \mathbf{A}(\mathbf{r}, t_{n-1})}{\Delta t^2} \right] dS \\ & + \int_S \mathbf{f}_m(\mathbf{r}) \bullet [\nabla \Psi(\mathbf{r}, t_n)] dS \\ & = \int_S \mathbf{f}_m(\mathbf{r}) \bullet \left[\frac{\partial \mathbf{E}^i(\mathbf{r}, t_n)}{\partial t} \right] dS. \end{aligned} \quad (14)$$

Now let us look at each term in Eq. (14), as follows:

Using Eq. (8), we can write vector potential term at any time instant as,

$$\begin{aligned} & \int_S \mathbf{f}_m(\mathbf{r}) \bullet \mathbf{A}(\mathbf{r}, t_n) dS \\ & = \int_{T_m^+} \frac{l_m}{2A_m^+} \boldsymbol{\rho}_m^+ \bullet \mathbf{A}(\mathbf{r}, t_n) dS \\ & + \int_{T_m^-} \frac{l_m}{2A_m^-} \boldsymbol{\rho}_m^- \bullet \mathbf{A}(\mathbf{r}, t_n) dS. \end{aligned} \quad (15)$$

The integrals will be approximated by evaluating $\mathbf{A}(\mathbf{r}, t_n)$ at the centroid of the T_m^\pm triangle. Therefore,

$$\begin{aligned} & \int_S \mathbf{f}_m(\mathbf{r}) \bullet \mathbf{A}(\mathbf{r}, t_n) dS \\ & \approx \left[\mathbf{A}(\boldsymbol{\rho}_m^{c+}, t_n) \bullet \frac{l_m}{2A_m^+} \int_{T_m^+} \boldsymbol{\rho}_m^+ dS \right. \\ & \left. + \mathbf{A}(\boldsymbol{\rho}_m^{c-}, t_n) \bullet \frac{l_m}{2A_m^-} \int_{T_m^-} \boldsymbol{\rho}_m^- dS \right]. \end{aligned} \quad (16)$$

The integrations in Eq. (16) are trivial and the result is given by:

$$\begin{aligned} & \int_S \mathbf{f}_m(\mathbf{r}) \bullet \mathbf{A}(\mathbf{r}, t_n) dS \\ & \approx \frac{l_m}{2} [\mathbf{A}(\boldsymbol{\rho}_m^{c+}, t_n) \bullet \boldsymbol{\rho}_m^{c+} + \mathbf{A}(\boldsymbol{\rho}_m^{c-}, t_n) \bullet \boldsymbol{\rho}_m^{c-}], \end{aligned} \quad (17)$$

where $\boldsymbol{\rho}_m^{c+}$ is the vector from the free vertex to the centroid of T_m^+ and $\boldsymbol{\rho}_m^{c-}$ is the vector from the centroid to the free vertex of T_m^- .

Next, let's consider the scalar potential term in Eq. (14). Using the vector identity $\nabla \bullet (\Psi \mathbf{A}) = \mathbf{A} \bullet \nabla \Psi + \Psi \nabla \bullet \mathbf{A}$ and using the properties of the RWG function \mathbf{f}_m , we have:

$$\begin{aligned} & \int_S \mathbf{f}_m \bullet \nabla \Psi(\mathbf{r}, t_n) dS = \\ & - \int_S \Psi(\mathbf{r}, t_n) \nabla \bullet \mathbf{f}_m(\mathbf{r}) dS. \end{aligned} \quad (18)$$

By approximating the integrand at the centroids of the triangles, Eq. (18) becomes.

$$\begin{aligned} & \int_S \mathbf{f}_m \bullet \nabla \Psi(\mathbf{r}, t_n) dS = \\ & - \left[\frac{l_m}{A_m^+} \int_{T_m^+} \Phi(\mathbf{r}, t_n) dS - \frac{l_m}{A_m^-} \int_{T_m^-} \Phi(\mathbf{r}, t_n) dS \right] \\ & \approx -l_m [\Phi(\boldsymbol{\rho}_m^{c+}, t_n) - \Phi(\boldsymbol{\rho}_m^{c-}, t_n)]. \end{aligned} \quad (19)$$

Finally, consider incident field term in Eq. (14). The evaluation of this term is identical to the vector potential term and the result is given by,

$$\begin{aligned} & \int_S \mathbf{f}_m \bullet \frac{\partial \mathbf{E}^i(\mathbf{r}, t_n)}{\partial t} dS = \\ & \frac{l_m}{2} \left[\frac{\partial \mathbf{E}^i(\boldsymbol{\rho}_m^{c+}, t_n)}{\partial t} \bullet \boldsymbol{\rho}_m^{c+} + \frac{\partial \mathbf{E}^i(\boldsymbol{\rho}_m^{c-}, t_n)}{\partial t} \bullet \boldsymbol{\rho}_m^{c-} \right]. \end{aligned} \quad (20)$$

C. Expansion procedure

Let us first look at the determination of the vector potential at some observation point $\mathbf{r} = \mathbf{r}_m$ at time $t = t_n$. Substituting Eq. (10) into Eq. (2) gives:

$$\begin{aligned}
 & \mathbf{A}(\mathbf{r}_m, t_n) \\
 &= \mu \sum_{p=1}^{N_S} \sum_{q=1}^{N_t} I_{p,q} \int_S \frac{\mathbf{f}_p(\mathbf{r}') g_q(t_n - \frac{|\mathbf{r}_m - \mathbf{r}'|}{c})}{4\pi |\mathbf{r}_m - \mathbf{r}'|} dS' \\
 &\approx \sum_{p=1}^{N_S} \sum_{q=1}^{N_t} I_{p,q} \\
 &\left[g_q(t_n - \frac{R_{mp}^+}{c}) \boldsymbol{\kappa}_{mp}^+ + g_q(t_n - \frac{R_{mp}^-}{c}) \boldsymbol{\kappa}_{mp}^- \right], \quad (21)
 \end{aligned}$$

with

$$\boldsymbol{\kappa}_{mp}^\pm = \int_{T_p^\pm} \frac{\mu \mathbf{f}_p^\pm}{4\pi R_m} dS', \quad (22)$$

$$R_{mp}^\pm = |\mathbf{r}_m - \mathbf{r}_p^{c^\pm}|, \quad (23)$$

$$R_m = |\mathbf{r}_m - \mathbf{r}'|, \quad (24)$$

where T_p^\pm represent the triangles connected to p^{th} -basis function.

Now, we consider the evaluation of the derivative of the scalar potential at some observation point $\mathbf{r} = \mathbf{r}_m$ and time $t = t_n$. Following steps similar to the evaluation of the vector potential, we combine Eqs. (5) and (10) to get:

$$\begin{aligned}
 & \Psi(\mathbf{r}_m, t_n) \\
 &\approx \sum_{p=1}^{N_S} \sum_{q=1}^{N_t} I_{p,q} \left[g_q(t_n - \frac{R_{mp}^+}{c}) \psi_{mp}^+ \right. \\
 &\quad \left. + g_q(t_n - \frac{R_{mp}^-}{c}) \psi_{mp}^- \right], \quad (25)
 \end{aligned}$$

where

$$\psi_{mp}^\pm = \frac{-I_p}{A_p^\pm} \int_{T_k^\pm} \frac{dS'}{4\pi \epsilon R_m}. \quad (26)$$

Using the expansion and testing procedures described so far, let us generate a matrix equation $\mathbf{Z}\mathbf{X} = \mathbf{Y}$ of dimension $P = N_S \times N_t$. The elements of the \mathbf{Z} -matrix are formed by using Eqs. (17), (19), (21) and (25). Note that $Z_{j,i}$ represents a matrix element of the \mathbf{Z} -matrix, where

$$\begin{aligned}
 j &= (n-1)N_S + m, & i &= (q-1)N_S + p, \\
 n, q &= 1, 2, \dots, N_S, & \text{and } m, p &= 1, 2, \dots, N_t.
 \end{aligned}$$

Here, we note that the \mathbf{Z} -matrix in this case is not a full matrix, unlike in the frequency domain MOM procedure. In fact, it is a lower triangular, block-wise Toeplitz matrix and given by,

$$\mathbf{Z} = \begin{bmatrix} \mathbf{Z}_{1,1} & \mathbf{O} & \cdots & \mathbf{O} \\ \mathbf{Z}_{2,1} & \mathbf{Z}_{2,2} & \cdots & \mathbf{O} \\ \vdots & \vdots & \vdots & \vdots \\ \mathbf{Z}_{N_S,1} & \mathbf{Z}_{N_S,2} & \cdots & \mathbf{Z}_{N_S,N_S} \end{bmatrix}, \quad (27)$$

where each $\mathbf{Z}_{m,p}$, $m = 1, 2, \dots, N_S$ and $p = 1, 2, \dots, N_S$ is a matrix of dimension N_S representing the mutual interaction between the spatial basis functions for a given pair of testing time function and source time function. The solution of such a matrix equation is very efficient, involves inverting only once a matrix of size $N_S \times N_S$, and solving the matrix equation.

The right hand side of the matrix equation \mathbf{Y} is obtained by using the Eq. (20) and consists of N_t blocks of matrices of dimension N_S . At this stage, we note that multiple incident pulses with varying frequency content can be easily accommodated by adding more column blocks to the \mathbf{Y} -matrix. Also, we note that obtaining currents for T to $2T$ and later instants is similar to solving the equation for 0 to T and presented in [20, 21].

Lastly, note that the numerical procedure presented so far allows to obtain the current distribution on the scattering structure as a function of time. Once an accurate current distribution is obtained, it is a simple process to obtain near-fields, far-fields, and any other required parameters. The mathematical details to obtain such parameters are well-known and available in [4] and hence not repeated here.

Before we present several numerical results obtained using the procedure presented so far, a few salient points must be noted as discussed in the following:

1. The first point to be noted is that the present procedure is *not* the same as the conventional MOT scheme although it might appear so for a casual reader. It is because, in the conventional MOT scheme, further mathematical manipulations are carried out wherein a MOT equation is developed to obtain the current at a present instant as a function of incident field plus currents at previous instants [4]. Hence, the numerical solution involves obtaining all the currents at a given instant before moving to the next instant. One cannot proceed to the next instant before completing the current calculations at the given instant because these currents are required for calculating the currents at next instant. This may be the primary cause for error accumulation and late-time instabilities. However, in the procedure presented in this work, we are actually solving the complete problem in a way wherein all the currents at all instants (*i.e.*, from 0 to T) are obtained at once. There is no time marching involved and, hence, no error propagation or accumulation.

2. In this work, we have used triangular functions to represent the time variable which is simple and efficient. However, it is also possible to use other functions such as Gaussian functions, as done in [21], Lagurre Polynomials or spline functions where the time-derivatives can be easily handled. The important points to be noted for this procedure is: application of the MOM procedure in space and time dimensions, solving for unknowns at all locations and all time instants simultaneously, and efficient numerical solution.
3. It may be noted that for time-domain calculations, it is customary to use a Gaussian pulse as the incident pulse since a true impulse cannot be generated numerically. Hence, it is always a good idea to estimate the frequency content in the selected time pulse for spatial discretization. The normal guideline in the solution of a time domain scattering problem is to obtain λ_{min} corresponding to the maximum frequency component in the incident pulse. Obviously, for a band-limited pulse λ_{min} is easy to obtain. For a Gaussian pulse, one needs to estimate the maximum frequency limit in a judicious manner. Then, it is necessary to make sure that all the edge lengths are sufficiently smaller (*i.e.*, less than one tenth of λ_{min}).
4. It should be further noted that a sloppy discretization would appear as growing instability even for the time period 0 to T . Fortunately, such discretization in the frequency domain problem simply generates an inaccurate result. However, in the time domain, one may see a completely unacceptable, an even misleading, solution. Hence, the spatial discretization must confirm to the prescribed limit.
5. It appears that the time domain solution is very sensitive to numerical processing and requires accurate evaluation of required quantities such as vector and scalar potentials. The numerical integrations must be carried out to a high degree of precision in each and every case.
6. The number of time functions to be used in the solution is not very critical, at least, for the excitation pulse used in this work. Here we emphasize that the time functions are used to represent the time variation in the interval 0 to T , where T represents the time instant at which time the incident field goes to zero. Note that the parameter T depends upon the pulse width

of the excitation pulse as discussed in the following:

IV. NUMERICAL RESULTS

In this section, we present numerical results for several conducting objects modeled by triangular patches. For all the examples presented in this section, the incident field given by,

$$\mathbf{E}^i(t, \mathbf{r}) = \mathbf{E}_o \frac{4}{T_P \sqrt{\pi}} e^{-\gamma^2}, \quad (28)$$

where

$$\gamma = \frac{4}{T_P} (ct - ct_o - \mathbf{r} \cdot \mathbf{a}_k). \quad (29)$$

In Eqs. (28) and (29), \mathbf{a}_k is the unit vector in the direction of propagation of the incident wave, T_P is the pulse width of the Gaussian impulse, $\mathbf{E}_o \cdot \mathbf{a}_k = 0$, \mathbf{r} is a position vector relative to the origin, c is the velocity of propagation in the external medium, and t_o is a time delay which represents the time at which the pulse peaks at the origin.

Initially, we present several examples showing the current density at a given location on the scatterer as a function of time and compare with the frequency domain MOM using the same spatial patch scheme and an inverse discrete Fourier transform (FD-IDFT). For these examples we have, referring to Eqs. (28) and (29), $\mathbf{E}_o = 120\pi \mathbf{a}_x$, $T_P = 4.0$ LM, $\mathbf{k} = -\mathbf{a}_z$, $ct_o = 1.5T_P$ LM, and $T = 2 * ct_o$. Note that 1 LM = 3.333 nSecs. The FD-IDFT solution is obtained by using 512 frequency samples in the 0 to 512 MHz range. We also note that sharper pulse can be used by adjusting the pulse width T_P .

As a first example, consider a square plate of 2.0×2.0 m, located in the XY -plane. There are 153

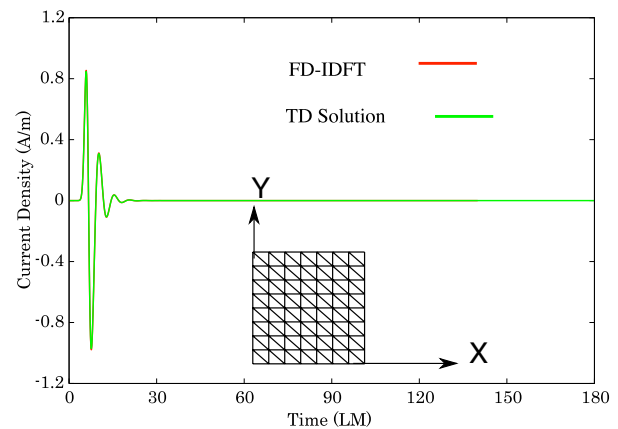


Fig. 3. Current induced at the center of a square plate ($L=2.0$ m) illuminated by a Gaussian plane wave.

and 108 basis functions for space and time variables,

respectively, for the time-domain solution. Note that, although 30 to 60 basis functions are sufficient for the time variable, we have deliberately used a higher number to show that the actual number of functions is not critical. For illustration purposes, the induced current density at the center of the plate is shown in Fig. 3. We note that the TD and FD-IDFT solutions compare very well for this case.

Next, we consider a sphere of radius 1.0 m, located with the center coinciding with the coordinate origin. The sphere is modeled with 722 triangular patches with 1083 spatial basis functions and 60 basis functions for time variable. For illustration pur-

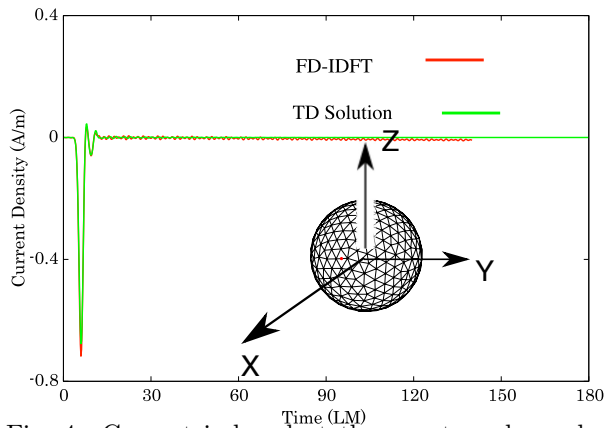


Fig. 4. Current induced at the equator, shown by a red dot, of a conducting sphere ($a=1.0$ m) illuminated by a Gaussian plane wave.

poses, the induced current density at the equator is shown in Fig. 4 and note that TD and FD-IDFT solutions compare very well.

Next, we consider a conducting cube of side length 1.0 m, located with the center coinciding with the coordinate origin. The cube is modeled with 224 triangular patches with 336 spatial basis functions and 60 basis functions in time. For illustration purposes, the induced current density at the center of the top face is shown in Fig. 5 and both solutions compare very well.

Next, we consider a combination of two square plates, each of side length $a = 1.0$ m and separated by a distance $d = 0.1$ m, located with the center of the bottom plate coinciding with the coordinate origin. Each plate is modeled with 112 triangular patches resulting in 366 spatial basis functions. The time-domain solution is obtained by employing 60 basis functions for the time variable. For illustration purposes, the induced current density at the center of the top plate is shown in Fig. 6 and note that the solutions compare very well. We note that the induced current oscillates for a long time because of

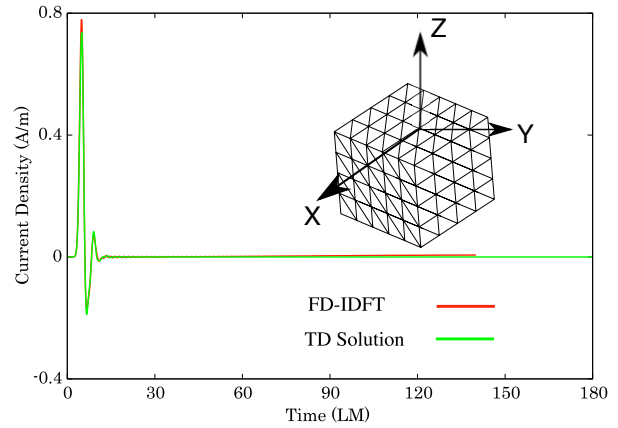


Fig. 5. Current induced at the center of the top face of a conducting cube ($a=1.0$ m) illuminated by a Gaussian plane wave.

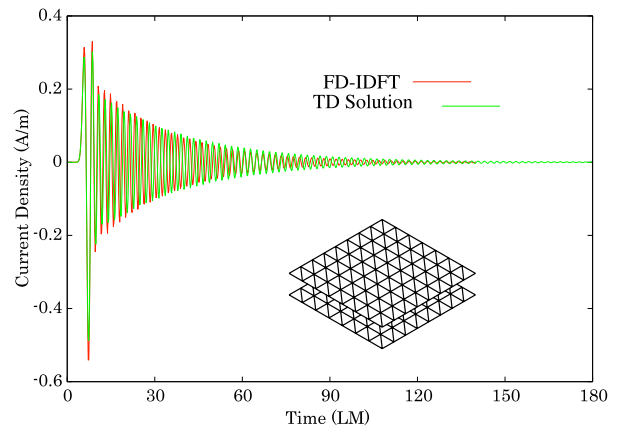


Fig. 6. Current induced at the center of the top plate of a parallel plate configuration ($a=1.0$ m, $d=0.1$ m) illuminated by a Gaussian plane wave.

the close proximity of the plates and the TD solution captures this phenomenon very well.

Now, we consider a combination of three square plates, each of side length $a = 1.0$ m and separated by a distance $d = 0.2$ m, located with the center of the center plate coinciding with the coordinate origin. Each plate is modeled with 180 triangular patches resulting in 753 spatial basis functions. The time variable is approximated with 60 functions. For illustration purposes, the induced current density at the center of the middle plate is shown in Fig. 7 and note that the solutions compare very well. It is obvious that this configuration represents a complex scattering structure from the scattering point of view. The electromagnetic wave bounces back and forth between the plates and takes a very long time to decay to a negligible value.

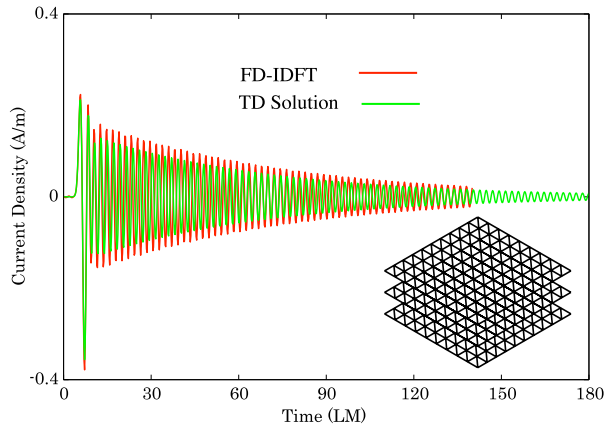


Fig. 7. Current induced at the center of the center plate of a 3-parallel plate configuration ($a=1.0$ m, $d=0.2$ m) illuminated by a Gaussian plane wave.

Next, we consider an almond-shaped structure described in the inset of Fig. 8. The almond is modeled with 432 triangular patches resulting in 648 spatial basis functions. The time variable is approximated with 60 functions. For illustration purposes, the induced current density at the center of the equator is shown in Fig. 8 and note that the solutions compare very well. It is well-known that the almond-shaped body represents a body with low radar cross section and the time domain solution performs very well for this case.

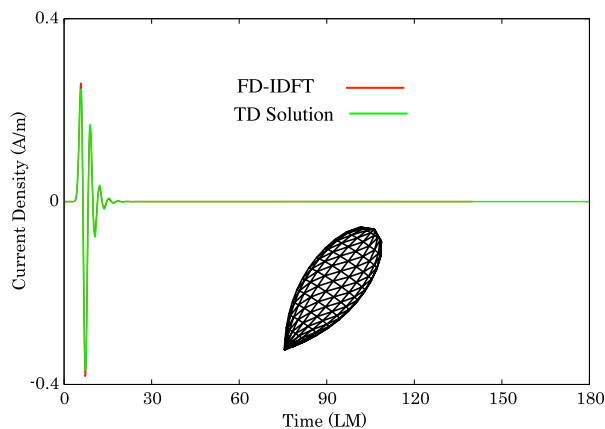


Fig. 8. Current induced at the center of the equator of an almond-shaped structure illuminated by a Gaussian plane wave.

Next, we consider an aircraft-like object, as shown in Fig. 9. The object is symmetrically placed in the XY -plane such that the center of the lower-side (belly) approximately coincides with the coordinate origin. The object dimensions are: 0.97 m, 0.86 m, and 0.25 m along the X , Y , and Z axes, re-

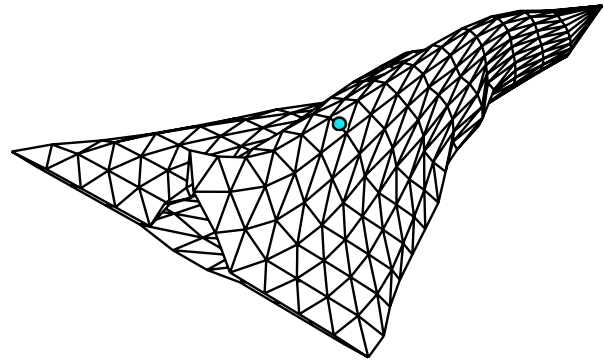


Fig. 9. An aircraft-like body modeled by triangular patches.

spectively. We have used 1000 and 48 basis functions for space and time variables, respectively. The current is sampled at the middle of an edge shown by a dot in the Fig. 9. The results obtained by FD-IDFT, and the present method are shown in Fig. 10. Again, we note good comparison between the two solutions.

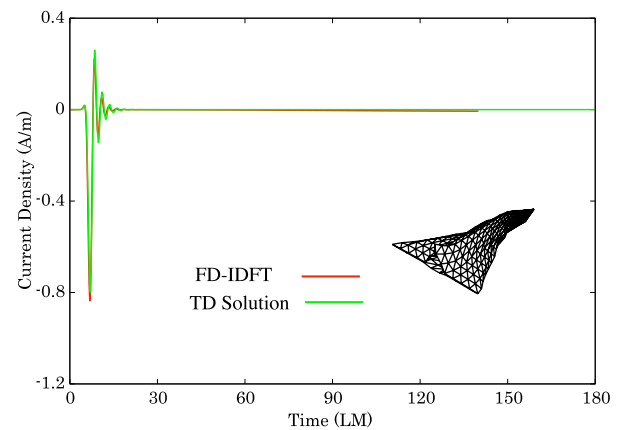


Fig. 10. Current induced on an aircraft-like structure illuminated by a Gaussian plane wave.

Next, we consider a more complex aircraft-like object, as shown in Fig. 11. The object dimensions are: 5.85 m, 3.5 m, and 1.46 m along the X , Y , and Z axes, respectively. We have used 2673 and 40 basis functions for space and time variables, respectively. The current is sampled on a wing, shown by a red dot, in the Fig. 11. The IDFT solution is obtained in a similar manner as in the previous example. The results obtained by FD-IDFT, and the present method are shown in Fig. 12. Again, we note good comparison between the two solutions. The negligible discrepancies in both solutions may be attributed insufficient number of unknowns at the higher end of the frequency.

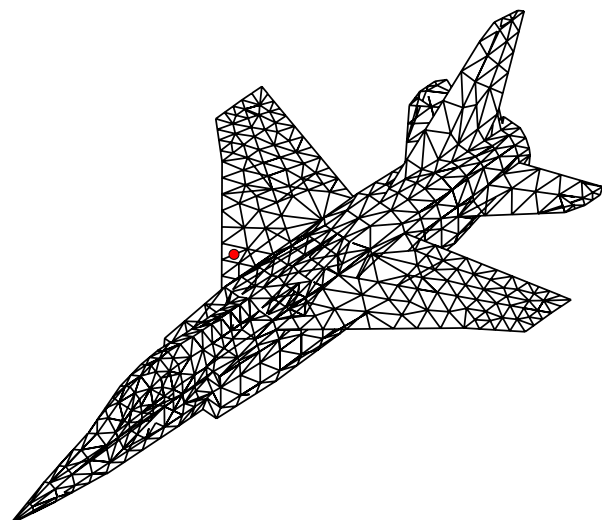


Fig. 11. Triangulated model of an aircraft-like body.

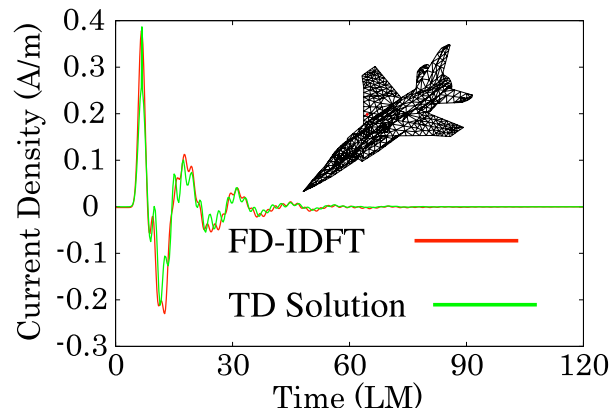


Fig. 12. Current induced on the wing of a model aircraft illuminated by a Gaussian plane wave.

Next, we consider a deep cavity as shown in the inset of Fig. 13. The depth of the cavity is 2.0 m. The inner and outer radii of cavity are 0.267 m and 0.4 m, respectively. The object is symmetrically placed in the XY-plane such that the center of the bottom surface coincides with the coordinate origin. We have used 552 and 40 basis functions for space and time variables, respectively. The current is sampled at an edge located in the inner surface at the bottom of the cavity. The results obtained by FD-IDFT, and the present method are shown in Fig. 13. Although we see a reasonable comparison, considering the complexity of the problem, it is speculated that neither solution is converged to the correct solution because of the coarse spatial sampling. The currents inside the deep zone are difficult to obtain and may require much higher number of unknowns.

Next, we consider a ship-like object, shown in

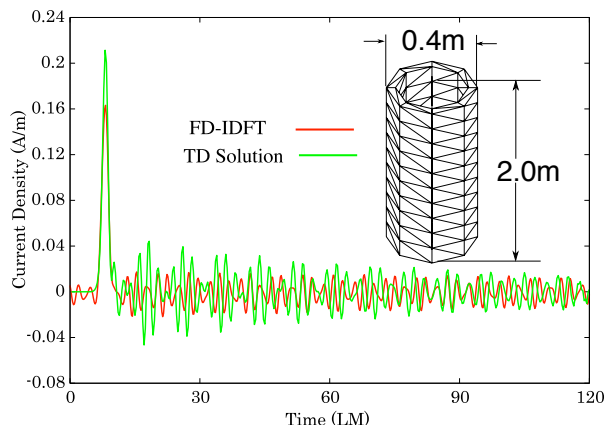


Fig. 13. Current induced on the bottom surface of a deep cavity illuminated by a Gaussian plane wave.

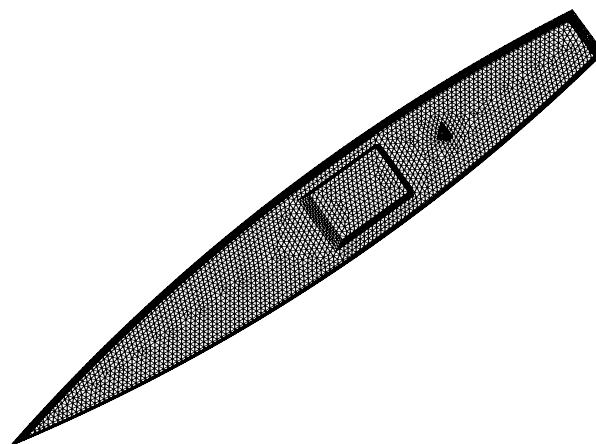


Fig. 14. Triangular patch model of a ship-like object.

Fig. 14. The ship is 5.56 m long, 0.716 m wide, and 0.387 m height and placed such that the origin is approximately coinciding with center of the top deck. There are 13,395 and 40 basis functions for space and time variables, respectively, for the time domain solution. The current is sampled at the middle of the upper-deck approximately coinciding with $x = y = 0$. The numerical results obtained by the method presented in this work is shown in Fig. 15. Also, note that IDFT solution for this example is prohibitively expensive and hence not attempted.

Now, we present radar cross section (RCS) of a few selected objects at a selected frequency using the time domain solution. Although, we can calculate RCS at any frequency within the pass band of the incident pulse, we choose a single frequency for illustration purposes. We note that once the induced current at all locations on a given object is obtained as a function of time, it is easy to use the straight-forward Fourier Transform method to ob-

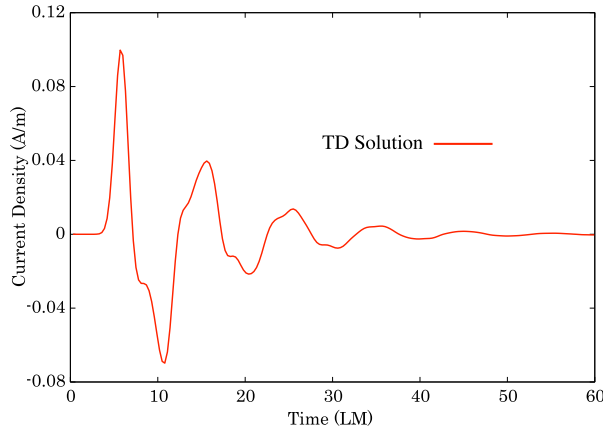


Fig. 15. Current at the selected point on the ship-like object modeled by triangular patches.

tain the currents at a given frequency. The Fourier transform for a time domain data may be defined as:

$$I_k(f) = \int_{t=0}^{\infty} i_k(t) e^{-j2\pi f t} dt, \quad (30)$$

where $i_k(t)$ is the current induced at k^{th} -basis function and f is the given frequency. Here, we note that the induced current is zero for $t < 0$.

Since the current data is obtained at equal time intervals, the integral in Eq. (30) may be easily approximated by:

$$I_k(f) = \sum_j i_k(j\Delta t) e^{-j2\pi f j\Delta t} \Delta t, \quad (31)$$

where Δt is the time interval. Next, the far-scattered electric field is obtained by the expression, given by:

$$\mathbf{E}^s(\mathbf{r}) = -j\omega\mu \frac{e^{-jk r}}{4\pi r} \int_S \mathbf{f}_k(\mathbf{r}') e^{j\mathbf{a}_k \cdot \mathbf{r}'} dS', \quad (32)$$

where \mathbf{f}_k represents the k^{th} -basis function, $\omega = 2\pi f$, $k = \frac{\omega}{c}$ is the wave number, \mathbf{a}_k represents the unit vector from the origin to the observation point, and c is the velocity of the electromagnetic wave.

Lastly, the radar cross section (σ) is given by,

$$\sigma(\theta, \phi) = \lim_{r \rightarrow \infty} 4\pi r^2 \frac{|\mathbf{E}^s|^2}{|\mathbf{E}^{inc}|^2} \quad (33)$$

which can be easily computed from Eq. (32) and the incident field given in Eq. (28).

In the following, we present normalized RCS (σ) at 900 MHz for four objects, *i.e.*, a) square plate, b) conducting sphere, c) a deep cavity and d) an aircraft-like body shown Fig. 9. We present two cases *viz.* a) Elevation cut (E-cut) where σ is obtained as a function of θ at $\phi = 0^\circ$ and b) Horizontal cut (H-cut) where σ is obtained as a function of ϕ at

$\theta = 90^\circ$. The time domain solution is obtained with a much sharper pulse with pulse width $T_p = 0.5$ LM providing a bandwidth from 0 to 1000 MHz. We also note that, the square plate, conducting sphere, deep cavity, and aircraft-like body have been approximated by 2628, 2160, 2208 and 4025 basis functions, respectively. The RCS plots are shown in Figs. 16, 17, 18 and 19. Although both solution compare well, the minor deviations may be attributed to the selected incident pulse in the time domain because at the selected frequency the amplitude of the incident pulse is quite low and hence, the normalization amplified the deviation even more.

V. CONCLUSIONS

In this work, a simple and efficient method of moments (MOM) solution procedure is developed to determine the transient scattering from arbitrarily shaped, conducting scatterers by a Gaussian incident pulse directly in the time domain. The scatterer may either be an opened or closed, finite three-dimensional object and described to the computer via planar triangular patch modeling scheme. The numerical solution scheme involves a straightforward method of moments application and requires no further mathematical manipulation. The MOM matrix thus generated is a lower triangular matrix which can be very efficiently filled because the matrix elements are also block-wise Toeplitz. As a result, the matrix equation can be very efficiently solved. Presently, work is in progress to apply the new method to material bodies.

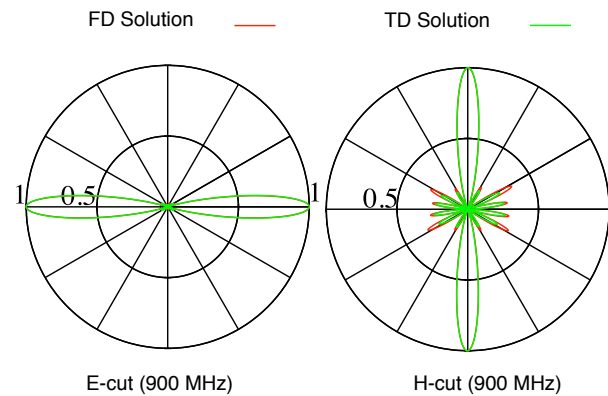


Fig. 16. Normalized bistatic RCS of a square plate (0.5×0.5 m) located in the XY -plane with center coinciding with the origin at 900 MHz. $N_S = 2628$.

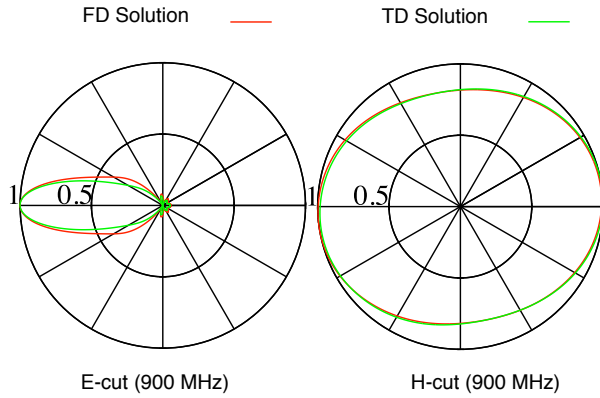


Fig. 17. Normalized bistatic RCS of a conducting sphere, radius=0.5 m, located with center coinciding with the origin at 900 MHz. $N_S = 2160$.

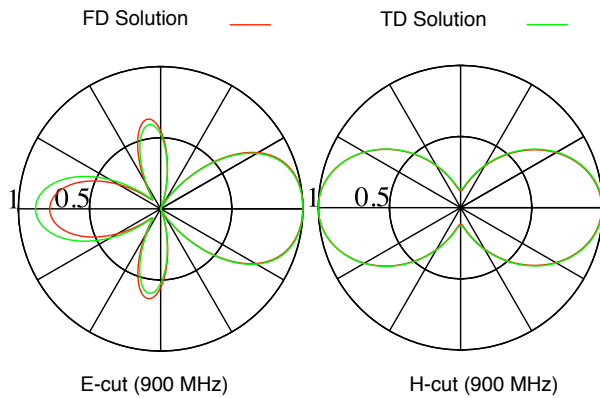


Fig. 18. Normalized bistatic RCS of a conducting cavity, length=0.25 m, inner and outer radii of cavity 0.08 m and 0.1 m, respectively, located with center coinciding with the origin, at 900 MHz. $N_S = 2208$.

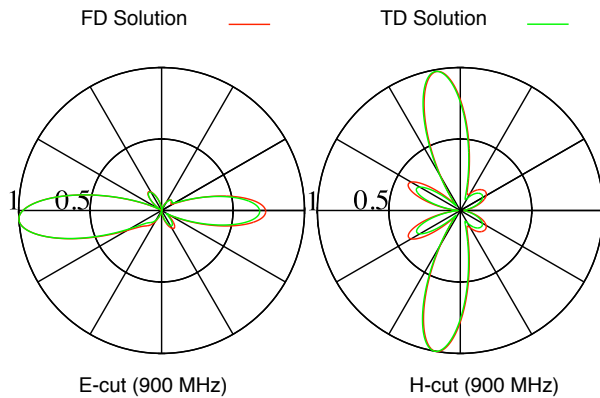


Fig. 19. Normalized bistatic RCS of an aircraft-like body, $N_S = 4025$.

ACKNOWLEDGEMENTS

This research was conducted under the Naval Research Laboratory Base Program sponsored by the Office of Naval Research.

REFERENCES

- [1] E. M. Kennaugh and R. L. Cosgriff, "The use of impulse response in electromagnetic scattering Problems," *IRE National Convention Record*, pp. 72- 77, 1958.
- [2] T. T. Wu, "A transient response of a dipole antenna," *Journal of Mathematical Physics*, vol. 2, Iss. 6, pp. 892- 894, 1961.
- [3] C. L. Bennett, *A technique for computing approximate electromagnetic impulse response of conducting bodies*," Ph.D. Thesis, Purdue University, August 1968.
- [4] S. M. Rao, *Time Domain Electromagnetics*, Academic Press, New York, 1999.
- [5] G. H. Zhang, M. Xia, and X. M. Jiang, "Transient analysis of wire structures using time domain integral equation method with exact matrix elements," *Progress In Electromagnetics Research*, vol. 45, pp. 281-298, 2009.
- [6] Y. Shi, M. Xia, R. Chen, E. Michielssen, and M. Lu, "Stable electric field TDIE solvers via quasi-exact evaluation of MOT matrix elements," *IEEE Transactions on Antennas and Propagation*, vol. 59, no. 2, pp. 574-585, February 2011.
- [7] H. A. Ulku and A. A. Ergin, "Application of analytical retarded-time potential expressions to the solution of time domain integral equations," *IEEE Transactions on Antennas and Propagation*, vol. 59, no. 11, pp. 4123-4131, November 2011.
- [8] B. H. Jung, Y. S. Chung, and T. K. Sarkar, "Time-domain EFIE, MFIE, and CFIE formulations using Laguerre polynomials as temporal basis functions for the analysis of transient scattering from arbitrarily shaped conducting structures," *Progress in Electromagnetics Research*, vol. 39, pp. 1-45, 2003.
- [9] B. H. Jung, T. K. Sarkar, Y. S. Chung, M. Salazar-Palma, and Z. Ji, "Time-domain combined field integral equation using Laguerre polynomials as temporal basis functions," *International Journal of Numerical Modeling: Electronic Networks, Devices and Fields*, vol. 17, pp. 251-268, 2004.

- [10] Y. S. Chung, T. K. Sarkar, B. H. Jung, M. Salazar-Palma, Z. Ji, S. M. Jang, and K. J. Kim, "Solution of time domain electric field integral equation using the Laguerre polynomials," *IEEE Transactions on Antennas and Propagation*, vol. 52, no. 9, pp. 2319-2328, September 2004.
- [11] Z. Ji, T. K. Sarkar, B. H. Jung, M. Yuan, and M. Salazar-Palma, "Solving time domain electric field integral equation without the time variable," *IEEE Transactions on Antennas and Propagation*, vol. 54, no. 1, pp. 258-262, January 2006.
- [12] N. J. Sekljic, M. M. Ilic, and B. M. Notaros, "Spatially large and temporally entire-domain electric field integral equation method of moments for 3-D scattering analysis in time domain," *IEEE Transactions on Antennas and Propagation*, vol. 63, no. 6, pp. 2614-2626, June 2015.
- [13] A. J. Pray, N. V. Nair, and B. Shanker, "Stability properties of the time domain electric field integral equation using a separable approximation for the convolution with the retarded potential," *IEEE Transactions on Antennas and Propagation*, vol. 60, no. 8, pp. 3772 - 3781, 2012.
- [14] Y. Beghein, K. Cools, H. Bagci, and D. De Zutter, "A space-time mixed Galerkin marching-on-in-time scheme for the time-domain combined field integral equation," *IEEE Transactions on Antennas and Propagation*, vol. 61, no. 3, pp. 1228-1238, March 2013.
- [15] Y. Beghein, K. Cools, and F. P. Andriulli, "A DC-stable, well-balanced, Calderon preconditioned time domain electric field integral equation," *IEEE Transactions on Antennas and Propagation*, vol. 63, no. 12, pp. 5650-5660, Dec. 2015.
- [16] Y. Beghein, K. Cools, and F. P. Andriulli, "A DC stable and large-time step well-balanced TD-EFIE based on quasi-Helmholtz projectors," *IEEE Transactions on Antennas and Propagation* vol. 63, no. 7, pp. 3087-3097, July 2015.
- [17] Z. He, H. H. Zhang, and R. S. Chen, "Parallel marching-on-in-degree solver of time-domain combined field integral equation for bodies of revolution accelerated by MLACA," *IEEE Transactions on Antennas and Propagation*, vol. 63, no. 8, pp. 3705-3710, August 2015.
- [18] Z. He, R. S. Chen, and W. E. I. Sha, "An efficient marching-on-in-degree solution of transient multi-scale EM scattering problems," *IEEE Transactions on Antennas and Propagation*, vol. 64, no. 7, pp. 3039-3046, July 2016.
- [19] M. D. Zhu, T. K. Sarkar, and H. Chen, "A stabilized marching-on-in-degree scheme for the transient solution of the electric field integral equation," *IEEE Transactions on Antennas and Propagation*, vol. 67, no. 5, pp. 3232-3240, May 2019.
- [20] S. M. Rao, "A stable marching-on-in-time algorithm capable of handling multiple excitations - application to wire junction problems," *IET Journal of Microwaves, Antennas and Propagation*, vol. 12, iss. 4, pp. 472- 478, 2018.
- [21] S. M. Rao, "A simple and efficient method of moments solution procedure for solving time domain integral equation - application to wire-grid model of perfect conducting objects," *IEEE Journal on Multiscale and Multiphysics Computational Techniques*, vol. 4, pp. 57- 63, 2019.
- [22] R. Harrington, *Field Computation by Moment Methods*, Macmillan, New York, 1968.
- [23] S. M. Rao, D. R. Wilton, and A. W. Glisson, "Electromagnetic scattering by surfaces of arbitrary shape," *IEEE Transactions on Antennas and Propagation*, vol. 30, pp. 409-418, 1982.